# On shape design and optimization of gerotor pumps

J. C. Pareja-Corcho[1,4] ⬤, M. Bartoň[2,3] ⬤, A. Pedrera-Busselo[5] ⬤, D. Mejia-Parra[1] ⬤, A. Moreno[1] ⬤, J. Posada[1] ⬤

[1]Vicomtech Foundation, Basque Research and Technology Alliance (BRTA), Mikeletegi 57, 20009 Donostia-San Sebastian, Spain
[2]BCAM – Basque Center for Applied Mathematics, Alameda de Mazarredo 14, 48009 Bilbao, Basque Country, Spain
[3]Ikerbasque – Basque Foundation for Sciences, Maria Diaz de Haro 3, 48013 Bilbao, Basque Country, Spain
[4]Faculty of Informatics, University of the Basque Country (UPV/EHU), Manuel Lardizabal 1, 20018 Donostia-San Sebastian, Spain
[5]Egile Innovative Solutions, Kurutz-Gain Pol. 12, 20850 Mendaro, Spain

## Abstract

*A gerotor pump is a two-piece mechanism where two rotational components, interior and exterior, engage each other via a rotational motion to transfer a fluid in a direction parallel to their rotational axes. A natural question arises on what shape of the gerotor is the optimal one in the sense of maximum fluid being pumped for a unit of time, given the constraint of a fixed material needed to manufacture the pump. As there is no closed-formula to answer this question, we propose a new algorithm to design and optimize the shape of gerotor pumps to be as efficient as possible. The proposed algorithm is based on a fast construction of the envelope of the interior component and subsequent optimization. We demonstrate our algorithm on a benchmark gerotor and show that the optimized solution increases the estimated flowrate by 16%. We also use our algorithm to study the effect of the number of teeth on the cavity area of a gerotor.*

**CCS Concepts**
• *Computing methodologies → Modeling methodologies;* • *Mathematics of computing → Mathematical optimization;* • *Applied computing → Computer-aided design;*

## 1. Introduction

Curved geometries appear in various industries, automobile sector being a prime example, where compact yet strong and efficient components are of a major importance. These object are, for example, components of car engines or gearboxes, and their performance affects the efficiency of the whole machine. An example of such a mechanical component, a gerotor pump, is shown in Fig. 1.

The gerotor pump, or *gerotor* in short, consists of two major components, the interior and the exterior parts, that are extrusions of 2D profiles in the direction of a common rotational axis. Both profiles are rotationally symmetric, however, their axis do not coincide but differ by the so called *eccentricity* distance. This axial deviation causes that, when properly designed, the internal component enrolls along the external counterpart in a hypocycloidal motion. The cavity between the two parts is filled by a fluid and, as the two parts engage each other, the fluid is pumped in a direction parallel to their rotational axes, as in Fig. 2.

Current trends in high-tech industry point towards new designs that allow using less material for components without compromising their quality or performance specifications. To make the manufacturing process as efficient as possible, one typically aims to maximize performance of the workpiece under constraints of the total material being used. In the context of gerotors, one may natu-
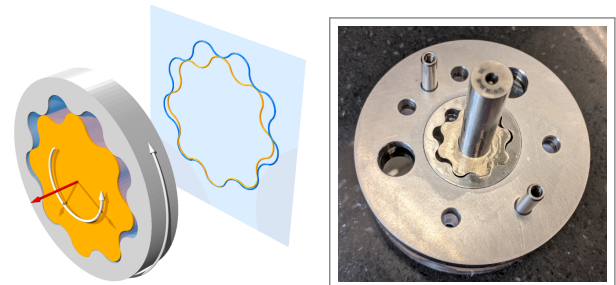


**Figure 1:** *Left: A gerotor pump consists of two major components, the interior and exterior part, that are extrusions of 2D profiles (yellow and blue) in the direction of the rotational axes (red). The two parts engage each other via a hypocycloidal motion which pushes the fluid through the cavities. Right: A real-life workpiece.*

rally ask about the optimal shape of the two components, as well as the optimal number of *teeth* that maximize fluid transfer under the weight and size constraints typical for this particular workpiece.

The proposed research studies this type of problem and proposes an optimization-based pipeline that looks for the most efficient gerotor. Our algorithm is based on several ingredients, namely
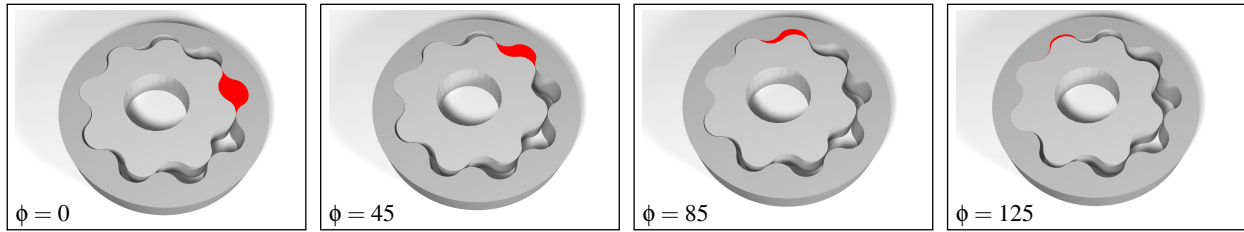
**Figure 2:** *Tracking of a single chamber (red) for the rotation of the pump by an angle ϕ. By rotating the internal part, the volume of the chamber compresses and pushes the fluid outwards in the direction of the rotational axis, recall Fig. 1.*

an efficient computation of the external profile of the pump (i.e. envelope of the internal profile), followed by the construction of the constraint manifold that corresponds to a fixed amount of material used for the internal profile, and finalized by a non-linear optimization. The main technical contributions of this paper are:

- An efficient algorithm to calculate the internal profile's envelope is proposed. We show that envelope points correspond to local extrema of a distance function from the instantaneous center of rotation, which simplifies considerably the outer profile construction and speeds up the whole gerotor design cycle.
- The search for the best shape of the gerotor is formulated as a constrained optimization problem, the physical feasibility of the gerotor being a pair of hypersurfaces, that delimit a search space in 3D, in which gerotors of constant material form a certain manifold. We build these manifolds in an efficient manner and explore them to find gerotors with maximum flowrate.
- The proposed algorithm is applied on an existing benchmark workpiece and increases its simulated flowrate by 16% while keeping the area (and weight) of the pump constant.
- Our optimization pipeline is run for several values of the number of teeth and confirms the engineering experience on the design of gerotor pumps, namely that the maximum eccentricity is strongly correlated with the maximum flowrate.

## 2. Related works

Gear sets that move fluids around have been studied and used for centuries: from the so called Archimedes pump [SH03] used in the ancient Nile, over the hydraulic gear sets used by Baron Armstrong in the bridges over the river Tyne in Victorian England [McN74], to the ever-smaller and ever-lighter gear pumps and engines of modern high-tech automotive [KPJ00, RN15], medical [LSTS*14, KGS15], and aerospace [IB12] industries. Given that gerotor pumps are relatively simple (only two moving parts), compact and robust, they have attracted a lot of attention in the past decade for industrial applications, see review papers on gerotor applications by Gamez-Montero et al. [GMCC19] and Rundo [Run17]. The related studies address mainly three major areas: design, simulation, and optimization.

*Design*. In theory any smooth, closed, and non-self-intersecting curve could define the internal profile of a gerotor pump. However, three main types are identified: *epitrochoidal* [PBS89], *hypotrochoidal* [HH07] and *cycloidal* [CKL*12]. All three are, however, based on the same principle: a moving circle rolls without slipping on the inside/outside of a static circle and a point on the moving circle traces the curve of the profile. See Robison and Vacca [RV21] for a comprehensive comparison and parametric expressions for all three types. Litvin and Feng [LF96] present the necessary conditions for the internal profile to be cusp-free and therefore usable for practical applications.

Once the internal profile has been defined, the external profile can be calculated in one of two ways: by a set of $Z$ circular arcs linked together in a central symmetric pattern, see Fabiani et al. [FMN*99]; or by the outermost envelope to the family of curves generated by the motion of the internal profile, see Yan et al. [YYT09]. The algorithms presented in this paper are developed using an hypotrochoidal (aka hypocycloidal) profile but are suitable for other types of profiles.

*Simulation*. Recent approaches to gerotor simulation use computational fluid dynamics to assess the performance of a particular design, see Altare et al. [AR16], Castilla et al. [CGMRC17], Pellegri et al. [PVF*17]. However, due to the high computational cost of CFD simulations, analytical methods have been developed to evaluate certain aspects of gerotor pumps without the need to resort to CFD-based models. These aspects include: flow estimation, see Lingeswaramurthy et al. [LJEK11]; forces and moments, see Ivanovic et al. [IDMC10]; and wear on profiles, see Kwon et al. [KKS08]. These analytical models respond to an constantly-growing trend in gerotor design and analysis, and in fact industry as a whole: the reduction of design, simulation, and fabrication time of to-be-manufactured components. Our paper addresses this very same issue from the perspective of geometrical optimization.

*Optimization*. Optimization techniques for gerotors have gained popularity in recent years. Several authors have contributed on optimization studies for gerotor shapes on hypocycloidal, see Kwon et al. [KKS11]; epitrochoidal, see Karamooz et al. [KRFM12]; or some rare assymetric profiles, see De Martin et al. [DMJS19]. These profiles are mostly optimized to reduce wear, flow irregularity and noise, see Robison et al. [RV18, RV19]. These approaches, however, are mainly focused on circular-based external profiles. We intend to maximize the flowrate by optimizing the shape of the gerotor using the envelope-based external profile.

Another related family of research deals with matching gears and/or screw rotors, see e.g. [KSS06, LF97, SSKM11, LF04] and other relevant references cited therein. A frequently used approach to design these pair mechanism is to design one part (male or female part in the case of screw rotors) and consider its relative mo-

tion with respect to the other, yet unknown part. This boils down to a 2D gearing problem. The other part is then defined as an envelope of the one-parameter family of positions of the first part under a cycloidal motion [SSKM11]. This approach has also been used recently for design of 2D gears [MSE20]. For two given 2D shapes to form a pair of non-circular gears, an optimization-based framework that looks for position of rotational centers that admit gearing configuration is presented in [XFS*20]. An algorithm to efficiently compute envelopes of moving solids is proposed in [SAJ21].

The rest of the paper is organized as follows. The modeling of gerotor pumps using cycloidal movements of circles is introduced in Section 3. The calculation of the external envelope is discussed in Section 4 and the shape optimization pipeline is presented in Section 5. The optimization results and benchmark comparison are presented in Section 6 and the limitations and concluding remarks are drawn in Section 7.

## 3. Geometric modeling of a gerotor pump

The internal profile of the gerotor is defined by a epicycloidal curve (i.e. the locus of a fixed point on a circle that rolls around another circle), see Robison and Vacca [RV21]; and the external profile can be constructed in one of two ways: by a set of circular arcs linked together in a central symmetric pattern, see Fig. 3(a); or by the *envelope* of the family of curves produced by the movement of the internal profile, see Fig. 3(b).
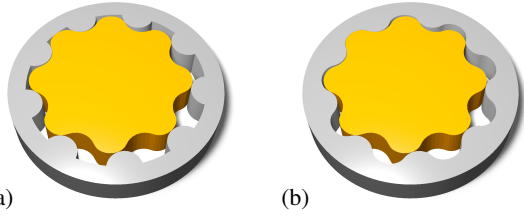
**Figure 3:** *Two types of external profiles are common in industrial gerotors: circular arc-based profile (left) and envelope-based profile (right). In this paper we focus on the envelope type profile.*

### 3.1. A hypocycloidal gerotor profile

The gerotor internal profile is formed by a hypocycloidal motion of two circles, see Fig. 4. The motion is determined by a movable circle $C_2$ rolling along a fixed circle $C_1$ without slipping. Circle $C_i$ ($i = 1, 2$) is defined by its center $\mathbf{O}_i$ and radius $r_i$. The centers of the circles are at all times separated by a constant distance $e$, known as the *eccentricity*, i.e., $\|\mathbf{O}_1 - \mathbf{O}_2\| = e$. Since the instantaneous center of rotation, $\mathbf{I}$, is the contact point of $C_1$ and $C_2$, it lies on the line $\mathbf{O}_1\mathbf{O}_2$.

Consider now a third circle $C_s$ lying in the moving frame, with a fixed position with respect to the movalble circle $C_2$. Let $\mathbf{P}_s$ be its center and $S$ its radius, recall Fig. 4. Consider the intersection point of the cirlce $C_s$ and the line $\mathbf{P}_s\mathbf{I}$, i.e., $\mathbf{r} = C_s \cap \mathbf{P}_s\mathbf{I}$. The motion of $\mathbf{r}$, as the $C_1$ and $C_2$ engage in a hypocycloidal motion, forms a curve, $\mathbf{r}(\theta)$, $\theta \in [0, 2\pi]$.

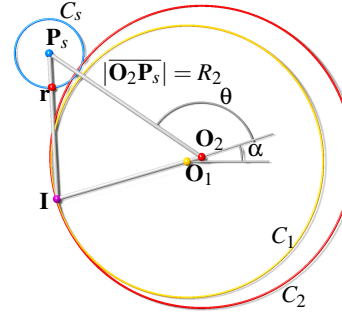When closing one turn of the hypocycloidal motion ($\theta \in [0, 2\pi]$),

**Figure 4:** *The gerotor internal profile is generated by a locus of points* **r** *as a movable circle* $C_2$ *engages a fixed circle* $C_1$ *in a hypocycloidal motion. Points* $\mathbf{O}_1$ *and* $\mathbf{O}_2$ *are separated by a fixed distance e (eccentricity).*

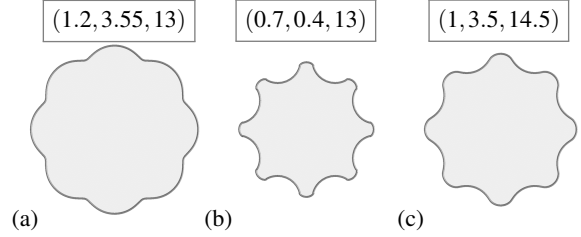$$(1.2, 3.55, 13) \quad (0.7, 0.4, 13) \quad (1, 3.5, 14.5)$$

**Figure 5:** *Effect of the shape parameters. Three different designs of the internal profile are shown. The framed triplets are the particular values of the free design parameters* $(e, S, R_2)$. *The number of teeth is* $Z - 1 = 8$ *in all three cases.*

the internal profile curve $\mathbf{r}(\theta)$ is required to be a closed curve, with a specfic number of *teeth*. Let $Z - 1$ be this number, then radii $r_1, r_2$, and $S$ have to satisfy certain constraints (otherwise $\mathbf{r}(0) \neq \mathbf{r}(2\pi)$), namely $r_1 = e(Z-1)$ and $r_2 = r_1 + e$ [MMRN00]. The choice of $Z - 1$ as the number of teeth of the internal gerotor profile is, as we will see later, in accordance with the fact that the external profile consists of $Z$ teeth.

Since the rolling without slipping is a composition of two rotations, two angles are needed to define the motion. Angle $\alpha$ defines the pure rotation of $\mathbf{O}_2$ around $\mathbf{O}_1$ and angle $\theta$ defines the rotation of circle $C_2$ around $\mathbf{O}_2$. The relationship between these two angles is given by $\theta = \alpha/Z$ and is set by the velocity condition for no-slipping rolling between the two circles.

Parametrizing the moving point $\mathbf{r}$, recall Fig. 4, one obtains

$$
\begin{aligned}
r_x(\theta) &= \cos(Z\theta)\left(e - \frac{Sr_2}{m}\right) - R_2\cos(\theta)\left(\frac{S}{m} - 1\right) \\
r_y(\theta) &= R_2\sin(\theta)\left(\frac{S}{m} - 1\right) - \sin(Z\theta)\left(e - \frac{Sr_2}{m}\right)
\end{aligned}
\tag{1}
$$

where

$$
m = \sqrt{R_2{}^2 + 2\cos(\theta(Z-1))R_2 r_2 + r_2{}^2}
$$

and $\theta \in [0, 2\pi]$. After replacing the definition of $r_2$ into Equation 1, we notice that the shape of the internal profile $\mathbf{r}(\theta)$ depends only on the eccentricity value $e$, length $R_2$, radius $S$ and the desired number of teeth $Z$ of the external profile. These *shape parameters* affect how the profile looks like, see Fig. 5, and consequently affect the performace of the whole pump. We aim to optimize the triplet of these shape parameters to find a profile that maximizes the performance of the pump. Before we get to the optimization, we need to describe how the external profile is generated, which we do next.

## 3.2. Planar kinematics of gerotors

As the gerotor operates, the internal profile defined by $\mathbf{r}(\theta)$ engages in epicycloidal motion with an external profile, see Fig. 6. To describe this movement we consider the curve $\mathbf{r}(\theta)$ as moving guided by the rolling without slipping of circle $C_1$ inside circle $C_2$, thus generating a one-parameter family of curves.
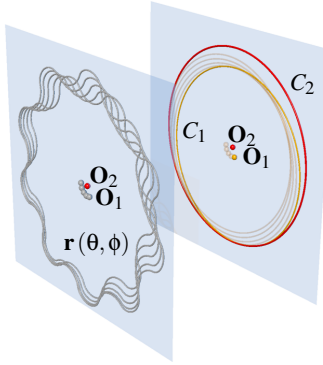


**Figure 6:** *Left: Five discrete samples ($\phi = 0$, 30, 60, 90, 120) from the family of internal profiles $\mathbf{r}(\theta, \phi)$ is shown. Right: The corresponding poisitions of circle $C_1$. For the whole (smooth) motion, $C_1$ moves along $C_2$ in a epicycloidal motion. The trajectory of $\mathbf{O}$ is a circle centered at $\mathbf{O}_2$ and with radius e.*

The rolling without slipping is defined as a composition of two rigid transformation $\mathbf{M} = \mathbf{M}_2(\phi)\mathbf{M}_1(\phi)$. As the motion depends on one parameter ($\phi$) and the internal profile is parametrized by another ($\theta$), the family of curves generated by the motion of $\mathbf{r}(\theta)$ can be interpreted as a bivariate vector function

$$\mathbf{r}(\theta, \phi) = \mathbf{T}_2^{\phi}(\mathbf{T}_1^{\phi}(\mathbf{r}(\theta))) \tag{2}$$

that is a composition of two transformations $\mathbf{T}_1^{\phi}$ and $\mathbf{T}_2^{\phi}$ (dependent on $\phi$) applied to $\mathbf{r}(\theta)$. The first transformation $\mathbf{T}_1^{\phi}$ is a rotation of $\mathbf{r}(\theta)$ around $\mathbf{O}_1$ followed by a translation by a vector $\mathbf{c}$, and the second transformation $\mathbf{T}_2^{\phi}$ is a rotation around the coordinate system of $\mathbf{O}_2$, that is,

$$\mathbf{T}_1^{\phi}(\mathbf{x}) = \mathbf{M}_1^{\phi}\mathbf{x} + \mathbf{c} \qquad \mathbf{T}_2^{\phi}(\mathbf{x}) = \mathbf{M}_2^{\phi}\mathbf{x} \tag{3}$$

where

$$\mathbf{M}_1^{\phi} = \begin{pmatrix} \cos(-\phi) & -\sin(-\phi) \\ \sin(-\phi) & \cos(-\phi) \end{pmatrix}, \quad \mathbf{M}_2^{\phi} = \begin{pmatrix} \cos(\frac{\phi(Z-1)}{Z}) & -\sin(\frac{\phi(Z-1)}{Z}) \\ \sin(\frac{\phi(Z-1)}{Z}) & \cos(\frac{\phi(Z-1)}{Z}) \end{pmatrix} \tag{4}$$

and $\mathbf{c}$ is the vector from $\mathbf{O}_2$ to $\mathbf{O}_1$, i.e., $\mathbf{c} = \mathbf{O}_1 - \mathbf{O}_2$.

## 3.3. Envelope of a family of curves

Consider a closed curve in $\mathbf{r}$ embedded in the two-dimensional Euclidean plane $\mathbb{E}^2$, $\mathbf{r} : I \to \mathbb{E}^2$, that undergoes a rigid body motion, parametrized by the motion parameter $\phi$. This motion can be interpreted as a bivariate vector-valued function $\mathbf{r}(\theta, \phi)$, recall Eq. (2).

A curve $\mathbf{e}$ that touches this one-parameter system of curves is called the *envelope* (of the system) [PP00]. Algebraically, this curve is one entity, however, in our applied problem, we should distinguish the branch that contains all the curves from the system. That is, we say that the $\mathbf{e}_o$ is the *outermost envelope* of $\mathbf{r}(\theta, \phi)$, iff $\mathbf{r}(\theta, \phi)$ is fully contained by $\mathbf{e}_o$, for all $\phi$. The inclusion is the classical inclusion in the context of two closed sets. To be well-defined, one needs to assume that the curve is closed and the motion also creates

a closed loop (and these assumptions are met in our gerotor pump case).

As a simple example of an envelope, one can think of an ellipse being rotated around a point that lies outside the ellipse. The envelope $\mathbf{e}$ is a pair of cocentric circles, and the outermost envelope $\mathbf{e}_o$ is the circle with the larger radius. For more complicated curves, the envelope can naturally have several branches (disconnected components), however, in our gerotor case, the envelope has only two branches, the internal and the external, see Fig. 7.
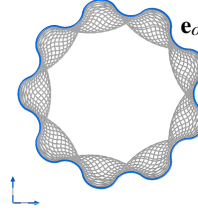


**Figure 7:** *Projection to the xy plane of $\mathbf{r}(\theta, \phi)$ (sampled by $\phi$-curves). The borders of the projected region are part of the envelope, but we are only interested in the outermost envelope $\mathbf{e}_0$.*

An interesting insight on construction of envelopes of 2D curves is as follows [PP00]: Consider the *xy*-plane that contains the internal profile, and the time $\phi$ as the third, vertical, axis. Then the motion of the curve can be visualized as a one-parameter family of curves in planes parallel to the *xy*-plane and the $\mathbf{r}(\theta, \phi)$ defines a surface, each horizontal slice of the surface being the position of the curve in the particular time instant $\phi$, see Fig. 8.

Angle $\phi = 0$ defines the initial position of the internal gerotor and $\phi = 2\pi \frac{Z}{Z-1}$ defines the next engaged position for the internal rotor. Setting $\theta = const$ retrieves a curve that corresponds to the trace of a single point in the gerotor profile as it moves under the rigid body motion.



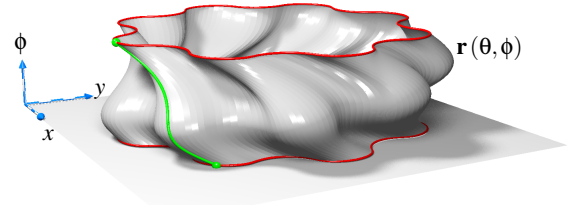**Figure 8:** *Spatial interpretation of the function $\mathbf{r}(\theta, \phi)$. The horizontal $\phi$-curves represent gerotor profiles at a particular time $\phi$; we show $\phi = 0, 2\pi \frac{Z}{Z-1}$ (red). The $\theta$-curve (green) represents the trace of a single point of the gerotor profile under the gerotor's motion.*

The tangent plane $T$ at any point of $\mathbf{r}(\theta, \phi)$ is spanned by the derivative vectors $\partial\mathbf{r}/\partial\phi$ and $\partial\mathbf{r}/\partial\theta$, i.e., its normal vector is $\mathbf{n}_T = \partial\mathbf{r}/\partial\phi \times \partial\mathbf{r}/\partial\theta$. For any point of $\mathbf{r}(\theta, \phi)$ to lie on the envelope, its tangent plane $T$ must project as a line into the *xy* plane [PP00], which is equivalent to $\mathbf{n}_T$ being parallel to the *xy* plane. This is true when the orthogonal complement of the motion derivative vector $(\partial\mathbf{r}/\partial\phi)^{\perp}$ is orthogonal to the angular derivative vector $\partial\mathbf{r}/\partial\theta$ (their dot product is zero), i.e,

$$\left\langle \frac{\partial\mathbf{r}(\theta, \phi)}{\partial\theta}, \frac{\partial\mathbf{r}^{\perp}(\theta, \phi)}{\partial\phi} \right\rangle = 0. \tag{5}$$

However, the envelope given by (5) may have several branches, recall Fig. 7, and we are only interested in the points on the outer-most branch $\mathbf{e}_o$ of the envelope $\mathbf{e}$. This outermost envelope forms the conjugated (matching) profile to the internal profile curve $\mathbf{r}(\theta)$, under the motion of the gerotor pump.

Since there is not a closed-form expression to retrieve this out-ermost envelope, we propose a numerical algorithm that calculates $\mathbf{e}_0$ efficiently.

## 4. Calculation of the external profile

In this section, we discuss the computation of the external part of the gerotor. As our objective is to optimize the shape of the whole gerotor, we need to calculate the external profile rather efficiently as it will be called in our optimization routine many times.

First of all, we exploit the fact that the object is rotationally sym-metric and therefore one can use only a certain part of the internal profile to compute the points of the envelope, and then apply rota-tion to complete the whole external profile. We define a *tooth pro-file* as the segment of the curve that contains a single convex and single concave region, see Figure 9. To characterize the geometry and kinematics of a whole gerotor, it suffices to study a single tooth profile.
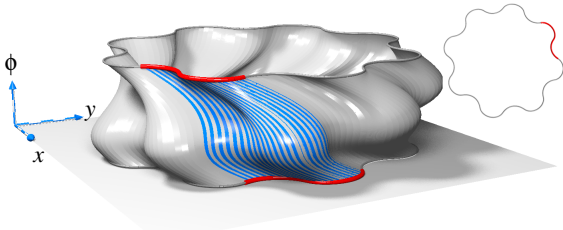


**Figure 9:** *The tooth profile (red) is the basic unit of symmetry in the gerotor. To study the motion of the internal profile it suffices to consider the motion (blue) of an internal tooth profile (red).*

Another important fact about gerotors is that an internal profile that has $Z-1$ teeth is matched with an external profile with $Z$ teeth, see Fig. 10 and e.g. [Col74]. Moreover, at each time instant, they stay in a tangential contact at $Z-1$ points, forming $Z-1$ chambers that transfer the fluid. Another fact is that each point of the internal profile $\mathbf{r}(\theta)$ will, at a certain time instant $\phi_i$, become a point of $\mathbf{e}_o$. This fact comes from the functionality of the gerotor and the fact that the chambers transfer the fluid by "pushing forward" the common point of tangency as the two profiles are being tangentially engaged one to another.

Consider now again the internal profile $\mathbf{r}(\theta)$ that consists of $Z-1$ repetitive teeth. Alternatively, one may segment $\mathbf{r}(\theta)$ into $2(Z-1)$ convex/concave segments, separated by the $2(Z-1)$ inflection points, see Figure 10.

To compute the envelope, consider Eq. (5), which gives all en-velope points (internal and external) and one needs to detect those points that can contribute only to the *outermost envelope*. Fixing $\phi$ and solving (5) for $\theta$, one obtains a set of stationary parame-ters (and consequently points) that can form the outermost enve-
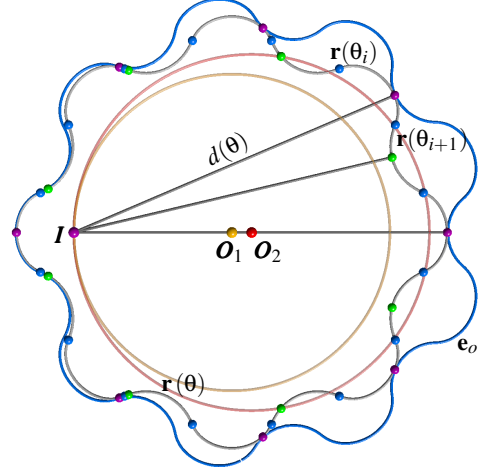


**Figure 10:** *Set of stationary points. These points can lie i) in the convex part of $\mathbf{r}(\theta)$ (magenta), ii) the concave part of $\mathbf{r}(\theta)$ (green), or iii) be inflection points of $\mathbf{r}(\theta)$ (blue). Line $\mathbf{Ir}$ is always normal to the time derivative vector $\partial\mathbf{r}/\partial\phi$.*

lope. These points can lie in i) the convex part of $\mathbf{r}(\theta)$, ii) the con-cave part of $\mathbf{r}(\theta)$, or iii) be inflection points of the curvature of $\mathbf{r}(\theta)$, recall Figure 10. This classification also corresponds to lo-cal minima, maxima, and inflection points of the distance function $d(\theta) := d(\mathbf{I}, \mathbf{r}(\theta))$ between the instantaneous center of rotation $\mathbf{I}$ and curve $\mathbf{r}(\theta)$, see Fig. 11.

The outermost envelope $\mathbf{e}_o$ is also a rotational symmetric closed curved. It consists of $2Z$ convex and concave segments. While the concave parts can be computed using both the convex and concave parts of $\mathbf{r}(\theta)$, the convex parts of $\mathbf{e}_o$ can be generated by only the convex points of $\mathbf{r}(\theta)$. This claim directly follows from the fact that $\mathbf{e}_o$ is the outermost envelope and has to be tangential to $\mathbf{r}(\theta)$. By contradiction, if some $\mathbf{r}(\hat{\theta})$ of the concave part of $\mathbf{r}(\theta)$ is also part of $\mathbf{e}_o$, then for arbitrarily small $\varepsilon \in \mathbb{R}$, $\varepsilon > 0$, the point $\mathbf{r}(\hat{\theta}\hat{+}\varepsilon)$ lies outside $\mathbf{e}_o$.

Therefore, to compute $\mathbf{e}_o$ it is sufficient to consider only the convex segment of $\mathbf{r}(\theta)$ between two inflection points $\mathbf{r}(\theta_i)$ and $\mathbf{r}(\theta_{i+1})$, which corresponds to the $\theta$ interval between two blue point, see Fig. 11; we take the interval that contains $\theta = 0$ value.

**Overview of the algorithm.** Consider now the internal profile at an initial time instant $\mathbf{r}(\theta, \phi = 0)$. Note that Eq. (5) is one semi-algebraic constraint in two variables and one could use a proper solver to numerically trace the solutions [BEH11]. However, such a global solver is an overkill as we do not need the internal branch, and would be non-trivial to exploit the symmetry. We already es-tablished that only convex parts of the curve $\mathbf{r}(\theta)$ will contribute to the outermost envelope, and that such an envelope can be char-acterized using a single tooth profile. Therefore we divide $\mathbf{r}(\theta, 0)$ into $2(Z-1)$ convex and concave segments. We select a convex segment, which we denoty by $\mathbf{r}^-(\theta)$ and proceed with a numerical tracing of a single solution branch [BEH11].

This curvature-based selection allows us to compute only the points on the outermost branch of the envelope and not all points
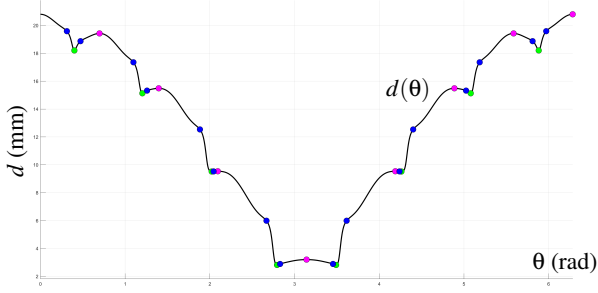
**Figure 11:** *Distance function $d(\theta)$ defined as the distance between instantaneous center of rotation $\mathbf{I}$ and $\mathbf{r}(\theta)$. Local maximizers (magenta), local minimizers (green), and inflection points (blue) are shown.*

that comply with Eq. (5) as many envelope algorithms (e.g. [PP00]) do. See Fig. 12 for a comparison between the solutions traced by our algorithm and those traced by [PP00]. Moreover, such an algorithm would need an a posteriori phase where the internal points are filtered out of the solution.
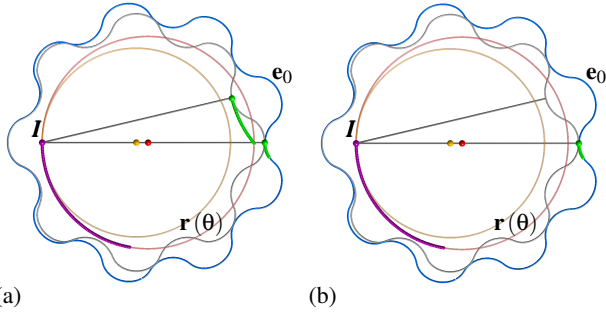


**Figure 12:** *Comparison between the root tracing in [PP00] (left) and ours (right) for $\phi \in [0, \pi/2]$. The solutions are shown in green. Our approach computes only the outermost branch of the envelope. Our approach executes this experiment in $t = 0.098s$ and the approach in [PP00] in $t = 0.55s$ for the same number of samples.*

For each time instant of $\mathbf{r}^-(\theta)$, the envelope point is updated and the outermost envelope $\mathbf{e}_0$ is calculated. Propagating in time, the sought-after segment of the envelope is an ordered sequence of points $\mathbf{e}_0 = \{\mathbf{p}_0, ..., \mathbf{p}_n\}$. Number $n$ denotes the number of desired points in the envelope's tooth profile and it is a parameter of our algorithm. Finally, we also know that the final point of the envelope's tooth profile $\mathbf{p}_n$ must be at an angle of $-\pi/Z$ with respect to the $x^+$ axis measured from the center $\mathbf{O}_2$; see Fig. 13.
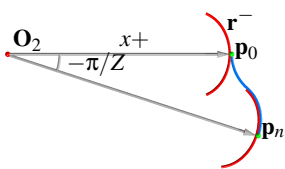


**Figure 13:** *Generation of the tooth profile for the external profile. Segment $\mathbf{r}^-$ moves according to the motion defined by parameter $\phi$ and in each time instant a new envelope point is calculated and added to the tooth profile (blue).*

**Envelope point update.** For each time instant $\phi$ a new enve-

lope point is calculated. The point must solve the envelope condition Eq. (5). We solve Eq. (5) in the convex segment defined by $\mathbf{r}^-(\theta, \phi)$. To solve this equation efficiently we use the previous envelope point as the initial guess for a Newton-Raphson method and, since we know that contact between $\mathbf{r}^-(\theta, \phi)$ and $\mathbf{e}_0$ is continuous, one looks in general for a single root of Eq. (5). For certain time instances, e.g., when the internal profile touches the inflection point of the outermost envelope, the corresponding parameter $\theta$ is a double root of Eq. (5). In such case, the Newton-Raphson converges only linearly to the root.

Recall that for any moving curve $\mathbf{r}(\theta, \phi)$, any vector normal to the time derivative vector $\partial \mathbf{r}/\partial \phi$ passes through the instantaneous center of rotation $\mathbf{I}$, recall Fig. 10. The calculation of the envelope can be further accelerated by considering the orthogonal complement of the derivative vector $\partial \mathbf{r}/\partial \phi$ (see Eq. (5)), which is the direction vector of the line $\mathbf{Ir}$. As one has $\mathbf{I}$ at hand, this fact eliminates the need to evaluate one of the derivatives. With this approach we ensure that the calculated points are on the envelope (up to the numerical precision, double-float in our implementation). At initial time $\phi = 0$, the central point of the convex segment $\mathbf{r}^-(\theta)$ is used as the initial guess.

**Resolution of the calculation.** Recall that curve $\mathbf{r}(\theta, \phi)$ moves guided by the hypocycloidal motion of circles $C_1$ and $C_2$ (recall Fig. 6). Therefore the instantaneous center of rotation $\mathbf{I}$ moves over circle $C_2$ as the motion evolves. For the initial time $\phi_0$, $\mathbf{I}$ will lie on the intersection between $C_2$ and the $x^-$ axis; and the final point $\mathbf{p}_n$ of the envelope $\mathbf{e}_0$ tooth profile will be calculated when $\mathbf{I}$ forms an angle of $\pi - \pi/Z$ with respect to the $x^-$ axis (or $-\pi/Z$ with respect to the $x^+$ axis), see Fig. 13. By setting the number $n$ of uniform samples as $\mathbf{I}$ sweeps the range $[0, \pi - \pi/Z]$ (from $x^-$ axis) we control the number of points calculated in the tooth profile of $\mathbf{e}_0$. The full envelope $\mathbf{e}_0$ will have then $N = 2Zn$ points.

## 4.1. Results of the envelope algorithm

The proposed algorithm to compute the outermost envelope for the given internal profile was thoroughly tested. A sample of the results for a fixed value $R_2$ and various shape parameters $e$ and $S$ is shown in Fig. 14 along with total area of the compression chambers, expressed as a percentage of the area of the internal profile. We set the number of points for a tooth profile as $n = 300$. The parameter values, together with the total number of points $N$ (full envelope) to approximate $\mathbf{e}_o$ and the total execution times are shown in Table 1. Observe that in average we need around $2s$ to compute the outermost envelope for $n = 300$. This is a sufficient accuracy as, for the typical size of a gerotor, $n = 300$ would translate into a resolution of a hundredth of a milimeter, fine enough resolution for manufacturing purposes and well within the capabilities of most CNC machines [Zha10].

We also studied how our algorithm scales with the desired number of points $n$ on the envelope's tooth profile, see Fig. 15. Our experiments show that the execution time scales *linearly* with $n$. Moreover, for a fixed $n$, due to the symmetry, the total number of points $N$ on $\mathbf{e}_0$ scales, as $Z$ increases, without a noticeable increase in the total computing time, see Table 1. Therefore, by setting $n$ (and this is usually a manufacturing-driven constraint) one could
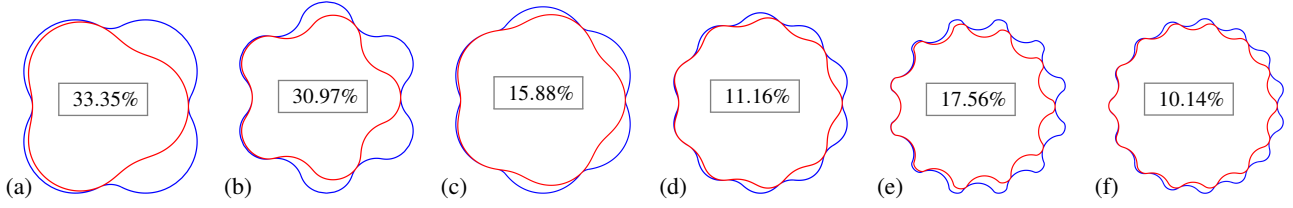
**Figure 14:** *Shapes of the internal profile* $\mathbf{r}(\theta)$ *(red) and outermost envelope* $\mathbf{e}_0$ *(blue) for different values of the shape parameters. The values of the shape parameters used are reported in Table 1. The framed values show the cavity area as a percentage of the internal gear's area.*

| Fig. 14 | $Z$ | $S$ | $R_2$ | $e$ | $t$ (s) | $N$ |
|---------|-----|-----|-------|-----|---------|-----|
| a | 4 | 3.5 | 15 | 1.7 | 2.8 | 2396 |
| b | 6 | 3.9 | 15 | 1.6 | 2.0 | 3594 |
| c | 6 | 2.0 | 15 | 0.9 | 1.9 | 3594 |
| d | 10 | 3.0 | 15 | 0.6 | 1.8 | 5990 |
| e | 12 | 3.0 | 15 | 1.0 | 1.8 | 7188 |
| f | 15 | 2.4 | 15 | 0.6 | 1.8 | 8985 |

**Table 1:** *Test of the envelope algorithm with different values of shape parameters. The shape parameters ($e$, $S$, $R_2$) used are reported along with the execution time $t$ and the number of points $N$ on the full envelope* $\mathbf{e}_0$. *Profiles are shown in Figure 14.*

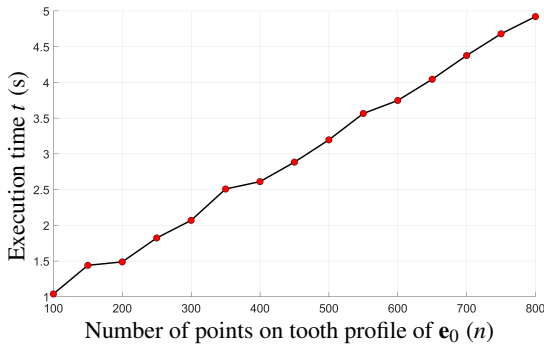calculate envelopes for any number of $Z$ with the same level of detail in the same time.



**Figure 15:** *Performance of our envelope algorithm depending on the desired number of points $n$ on the outermost envelope* $\mathbf{e}_0$'s *tooth profile for a fixed triplet* $(e, S, R_2)$.

## 5. Gerotor shape optimization

We aim to optimize the set of shape parameters of an existing gerotor pump to maximize the fluid pumped by the gerotor for a unit of time. The problem is well-posed under the constraint of a fixed area/volume of the internal profile, which is proportial to the weight of the pump and also reflects a fixed amount of material needed to manufacture the pump. This requirement heavily constrains the search space but it is a common requirement in engineering scenarios where a more efficient pump is needed to replace a pump that already exists within a system with limited space and weight limits.

We also restrict the pump's change in diameter to $\pm 1$ mm to ensure that the optimized pump does not change much in total diameter with respect to the original workpiece.

### 5.1. Area of internal profile

As already mentioned, the gerotor is a 2D mechanism extruded in the direction perpendicular to its plane and therefore the constraint on constant volume is equivalent to the constraint of constant area of the 2D analogue. To approximate the area of the gerotor, one has to discretize it. Even though we have the parametrization of $\mathbf{r}$, and one could consider using the Green's theorem to compute the area, the formula contains terms that cannot be integrated symbolically and one would have to compute the integral numerically anyway. Therefore, we approximate the area enclosed by $\mathbf{r}$ directly using a sum of triangles.

We approximate the area enclosed by the internal profile $\mathbf{r}(\theta)$, which is a function of three shape parameters $e$, $S$ and $R_2$. Consider a point $\mathbf{r}_1 = \mathbf{r}(\theta_1)$ and a point $\mathbf{r}_2 = \mathbf{r}(\theta_1 + \delta)$. The area of the triangle $\triangle \mathbf{O}_1 \mathbf{r}_1 \mathbf{r}_2$ formed by the center of the rotor $\mathbf{O}_1$ and the two points $\mathbf{r}_1$ and $\mathbf{r}_2$ is given by

$$A_\triangle(\theta_1, \delta) = \frac{1}{2} \mathbf{r}_1 \times \mathbf{r}_2. \tag{6}$$
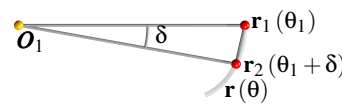


**Figure 16:** *The area of triangle* $\triangle \mathbf{O}_1 \mathbf{r}_1 \mathbf{r}_2$ *approximates the area enclosed by the segment of the gerotor between* $\mathbf{r}_1$, *and* $\mathbf{r}_2$.

To calculate the area we again exploit the fact that the gerotor is rotationally symmetric. The area of the full gerotor corresponds to $(Z-1)$ times the summation of the areas of all triangles as $\theta$ sweeps the range of a single tooth profile. Recall from Fig. 9 and 10 that a tooth profile is defined as the portion of $\mathbf{r}(\theta)$ given by two consecutive convex and concave segments. Therefore we sample the range of a single tooth profile by $k$ samples, i.e. $\theta_{i+1} = \theta_i + \delta$, $i = 1, \ldots, k-1$. Denoting the total area by $G$, we get

$$G(\delta) = (Z-1) \sum_{i=1}^{k-1} A_\triangle(\theta_i, \delta). \tag{7}$$

Observe that $G$ depends on the discretization stepsize $\delta$ (controled by $k$) and also on the initial $\theta$ that we set $\theta_1 = 0$. The $\delta$ parameter

governs the accuracy of the approximation. To measure the accuracy of our estimation with respect to the numerical integration via Green's theorem we calculate the mean absolute error (MAE) for the area calculation of the internal profiles shown in Fig. 14, see Fig. 17. This plot shows the error behavior as a function of the stepsize $\delta$. Based on this function, one can estimate a safe stepsize $\widetilde{\delta}_0$ such that our direct approach via discretization of the internal profile returns the same error as numerical integration targeting double-float precision. The threshold that keeps highly-accurate area computation is $\widetilde{\delta}_0 = 10^{-6}$ and therefore we set $\delta$ to this value in our algorithm.
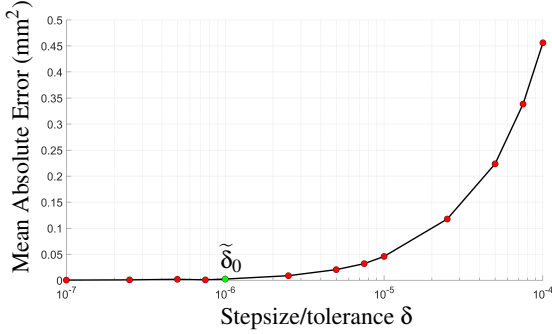


**Figure 17:** *Mean Absolute Error (MAE) calculated for the area estimation of the profiles in Fig. 14. We choose our stepsize as $\widetilde{\delta}_0 = 1 \times 10^{-6}$ (green).*

Note that $G$ also depends on the three shape parameters $e$, $S$ and $R_2$, and the number of teeth of the internal profile $Z - 1$. Fixing the number of teeth, $G = const.$ can be interpreted as an implicit surface in the $(e, S, R_2)$-shape space, see Fig. 18. Observe that Eq. (7) can be differentiated with respect to the shape parameters $e$, $S$ and $R_2$ to obtain a gradient vector $\nabla G$. In the optimization of non-analytic objective functions, at every time-step the gradient of the objective function $F$ is estimated by searching using finite-differences to look for the cheapest direction. Since deviation from the constraint manifold will be penalized in the objective function, by using the constraint gradient one can rapidly discard search directions that deviate from the constraint manifold without the need to evaluate the objective function $F$, thus accelerating the convergence towards the optimizer. This is another reason why we compute the area via direct discretization of the curve, rather than the Green's theorem and numerical integration.

### 5.2. Physical feasibility

To define a physically feasible interior gerotor profile $\mathbf{r}(\theta)$, the tangent vectors at every point must be uniquely defined, i.e. there must not be *singular* points, as singular points represent features such as cusps or self-intersections, which makes the profile unfeasible for practical applications, see Fig. 19. The feasibility of $\mathbf{r}(\theta)$ can be assured by adequate relationships between the shape parameters

$$\frac{r_2 (\lambda - 1)^3 (\tau - 1)}{(\tau - 1) \lambda^2 + (1 - 2\tau) \lambda + \tau} \leq S \leq \frac{3\sqrt{3} \sqrt{R_2^2 - r_2^2} (\tau - 1)}{(2\tau - 1)^{3/2}} \quad (8)$$

where $\lambda = R_2/r_2$ and $\tau = Z/(Z - 1)$. For more details about derivation of Eq. (8) see [LF96, Section 5]. Since circle radius $r_2$ can
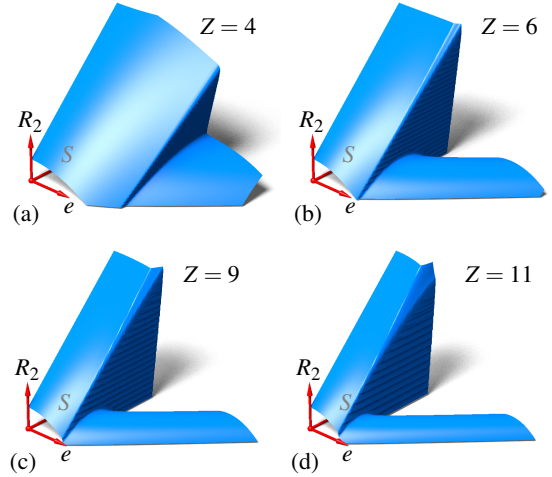


**Figure 18:** *Implicit surfaces generated by the fixed area constraint $G(e, S, R_2) = const.$ for different values of the number of teeth. For all cases we use a fixed area of const. $= 390 \ mm^2$ and ranges of interest for the shape parameters: $(e, S, R_2) \in [0, 5] \times [0, 5] \times [11, 15]$.*

be calculated from $e$ and $Z$ (recall the profile construction in Section 3.1), the feasibility condition depends only on the shape parameters $e$, $S$, $R_2$ and the desired number of teeth $Z$.
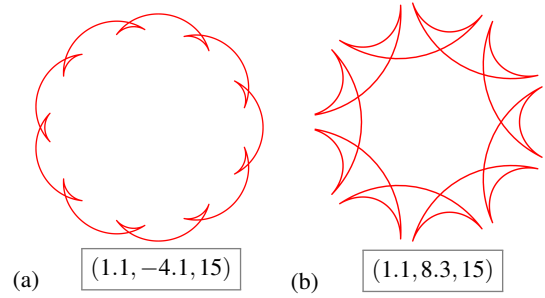


**Figure 19:** *The violation of the feasibility condition (Eq. (8)) results in profiles that contain cusps and self-intersections, and are not suitable for practical applications. The boxed values show the triplets $(e, S, R_2)$.*

Given a fixed $Z$, the constraint in Eq. (8) defines a subset of the shape parameter space. We call this subset the *feasible space* and denote it by $\Omega_f$, see Fig. 20. $\Omega_f$ is delimited by the boundary surface defined in Eq. (8) (when the equality holds) and contains all triplets $(e, S, R_2)$ that generate valid profiles.

### 5.3. Shape optimization

As the gerotor's flowrate is proportional to the total size of the compression chambers [LKSK18], to find the most efficient gerotor, we optimize the profile design parameters to maximize the sum of areas of all chambers. This area is the difference between the areas enclosed by the external and the internal profile (recall Eq. (7)). The search for the optimal gerotor mechanism is formulated as an
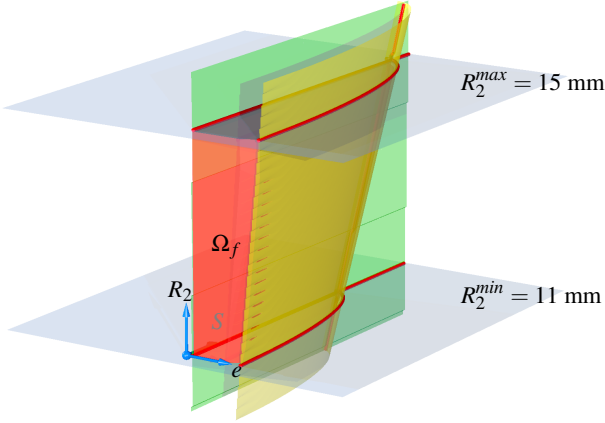
**Figure 20:** *The feasible space $\Omega_f \subset \mathbf{R}^3$ (red) is delimited by the feasibility constraint surfaces of Eq. (8) (yellow and green), the $R_2^{min}$ and $R_2^{max}$ planes (blue) and constraints $e > 0$ and $S > 0$. Every point $\boldsymbol{g} \in \Omega_f$ corresponds to a physically feasible gerotor.*

optimization problem:

$$\max_{e,S,R_2} F(e,S,R_2) = A_{ext}(e,S,R_2) - G(e,S,R_2) \qquad (9)$$

subject to two constraints:

$$G(e,S,R_2) - const. = 0 \quad \text{and} \quad \text{Eq. (8)}, \qquad (10)$$

where the first constraint is the condition of a fixed area of the internal profile and the second constraint is the physical feasibility, discussed in Section 5.2. The objective function $F$ expresses the cavity area of the gerotor (i.e. available area to be filled with fluid).
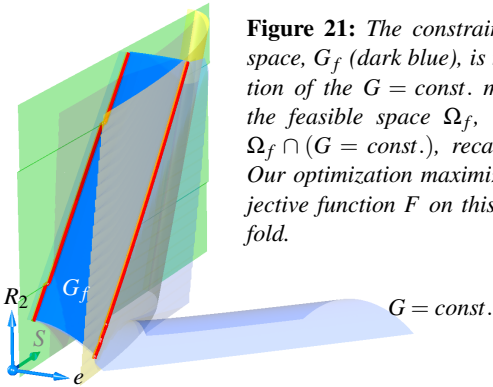


**Figure 21:** *The constrained search space, $G_f$ (dark blue), is the restriction of the $G = const.$ manifold to the feasible space $\Omega_f$, i.e., $G_f = \Omega_f \cap (G = const.)$, recall Fig. 20. Our optimization maximizes the objective function $F$ on this $G_f$ manifold.*

**Remark 1.** *The external part of a gerotor pump is built using not only the external envelope, but also an external circle, recall Fig. 3, of a given radius $R_{ext}$. This circle defines the size of the overall set and one should consider it when calculating the weight. The material area of the whole gerotor is then $\pi R_{ext}^2 - F$. However, even though the value of $R_{ext}$ is proportional to the areas of the internal and external profiles, it is primarily defined by engineering constraints (e.g. interface of the gearset with the machine assembly). As it is not possible to consider these constraints in our optimization pipeline, we define our constant weight ($\equiv$ material) constraint*

as the area of the internal profile constant ($G = const.$). An exploration of the constraint manifold is shown in Fig 22.
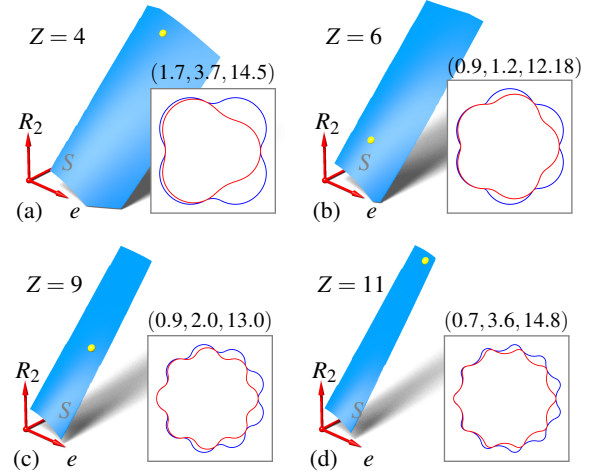


**Figure 22:** *Constrained search space $G_f$ (blue) for various values of Z. The feasibility space $\Omega_f$ shrinks for increasing Z, resulting in smaller manifolds $G_f$. The framed images show the profiles corresponding to the marked point (yellow) on the constraint manifold. The triplets $(e, S, R2)$ are shown for each case.*

To solve the optimization problem we opted for an interior point algorithm [WMNO06]. In this implementation the implicit surface constraint, which is characterized as a nonlinear equality constraint, is managed through a logarithmic barrier function and its gradient function used to speed up convergence, see [CGT97]. The feasibility nonlinear inequality constraints are managed using penalty multipliers [Deb00]. When one wants to optimize an existing piece, the $(e, S, R_2)$ triplet of the original gerotor can be set as the initial point $\boldsymbol{x}_0$ for the interior point algorithm. When no original piece exists, we opt for an Augmented Lagrangian Genetic Algorithm [CGT97] to produce an initial guess $\boldsymbol{x}_0$ in the constraint manifold and then we refine the best solution obtained by the genetic algorithm using the same interior point algorithm.

## 6. Results and benchmark comparison

To test our methodology we optimize an existing workpiece. We aim to maximize the fluid's area of the pump for the same number of teeth $Z = 9$ and keep the internal area of the workpiece constant and the radius $R_2$ in the range $[13, 14]$ mm. The profiles of the original workpiece and the optimized profiles, along with their corresponding shape parameters, are shown in Figure 23. The optimized piece mantains the same area for the internal gear as in the original piece but produces larger compression chambers. This increased volume capacity translates into a higher flowrate of the optimized piece while keeping the same gear area, and therefore the material needed for its fabrication.

To validate our optimization, we calculate explicitly (with 5000 samples) the constrained search manifold $G_f$ for the original workpiece and evaluate *in extenso* the objective function $F$ (cavity area) over the whole manifold. Fig. 24 shows three points on $G_f$ that

represent to the original workpiece, the optimized gerotor and the shape that corresponds the mean value of $F$ throughout $G_f$. We also show the location of the maximum-valued $P_{max}$ gerotor computed using the sampled manifold. The maximum value of $F$ estimated using our optimization pipeline $F(P_{opt}) = 92.47$ mm$^2$ differs from that of the maximum in the sampled manifold $F(P_{max}) = 92.36$ mm$^2$ by 0.11%. Notice that the total execution time to evaluate in extenso the sampled constraint manifold takes over two hours (7810 seconds) while our optimization pipeline runs in under two minutes.
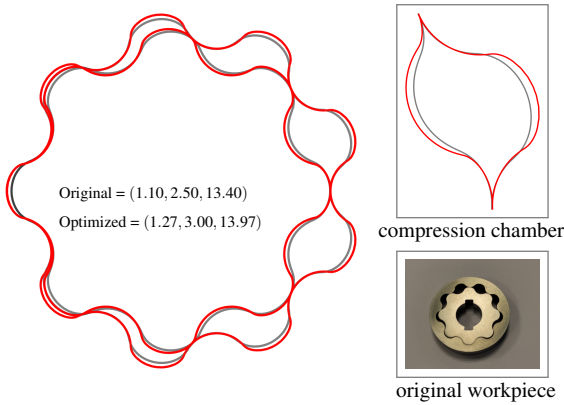


**Figure 23:** *Gerotor profiles (both internal and external) of the original shape (black) and the optimized pump (red) are shown. The area of the internal profile is 377.59 mm$^2$ in both cases. The increased compression chamber at one particular time instant is zoomed-in; the set of original and optimized parameters $(e, S, R_2)$ are shown.*

We also estimate the instantaneous flowrate (amount of fluid per unit time) of each pump to demonstrate that our optimized profile is better than the original workpiece, see Fig. 25. We do this by a numerical method (see Rundo [Run17, Section 4.2]) that calculates the area of the compression chambers for each time instant the pump. We perform all estimations for a pump speed of 10000 rpm and we show that the optimized profile increases the mean estimated flowrate $q_{avg}$ of the existing workpiece from 7.44 lpm (liters per minute) to 8.62 lpm, an increase of 15.88%. Comparing the optimized profile to the pump corresponding to the mean-value of $F$, the increase in the mean flowrate is of 70.25%.

Fig. 26 shows the evolution of the area for a single compression chamber in time in the case of the original profile and the optimized profile. The increase in the flowrate corresponds to the increase of available fluid amount in each chamber and one can see that the optimized chamber absorbs, at every time instant, more fluid than the original profile.

We use our optimization pipeline to study the effect of the number of teeth $Z$ on the gerotor's cavity area. We find the optimum $P_{opt}$ profile for $Z = [7, 8, 9, 10]$ for the same internal area as our original workpiece (377.59 mm$^2$). In Fig. 27 we show the optimum profiles, their location on the constraint manifold, and the *in extenso* evaluation of the manifolds sampled with 5000 points. Observe that the maximum cavity area diminishes as $Z$ increases. We also note that, for all values of $Z$, the cavity area increases as the eccentricity $e$ increases. This is in accordance with the engineering practice,
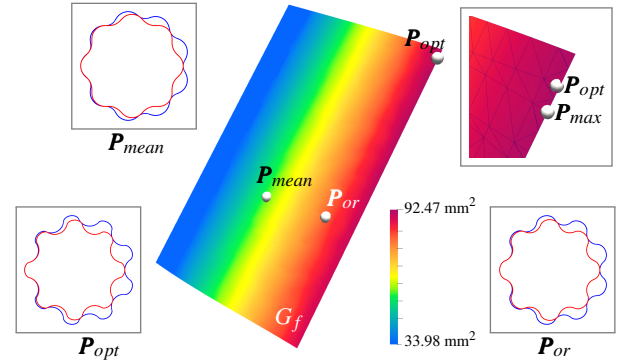


**Figure 24:** *Constrained search space $G_f$ for the optimization of the original workpiece. We evaluate objective function $F$ in the entire manifold with 5000 samples. We show the locations on the manifold of the original gerotor $P_{or}$, the optimized version $P_{opt}$, the maximum-valued gerotor $P_{max}$, and the mean-valued gerotor $P_{mean}$ computed over the sampled manifold.*
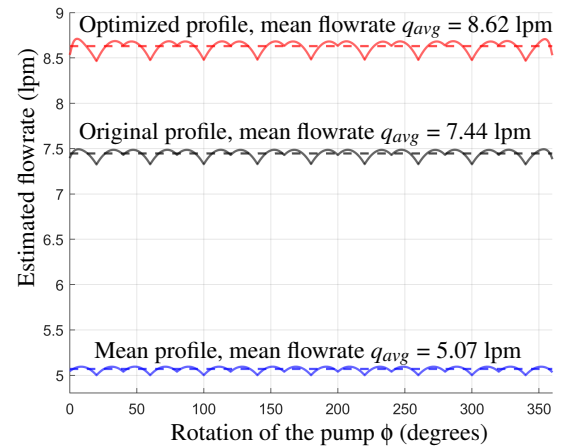


**Figure 25:** *Estimated instantaneous flowrates for the original (black), optimized (red) and mean (blue) pumps in a full cycle. The mean flowrate (dotted lines) of the increased from 7.44 lpm of the original pump to 8.62 lpm of the optimized pump, which corresponds to an increase by 16% in the total flowrate of the pump.*

and also the experience of our industrial partner (Anonymous), that increasing the eccentricity increases the flowrate.

## 6.1. Implementation details

The whole algorithm was implemented in MATLAB and the MATLAB's integrated optimization toolbox was used to solve the optimization problem posed. All tests were conducted in a computer with 16 GB RAM and 11th Gen Intel Core i5-11400 (2.6GHz) processor. The execution times for the envelope algorithm were reported in Table 1 and Fig. 15. The execution times for the entire optimization pipeline in the case of the examples presented in Fig. 27 are reported in Table 2.
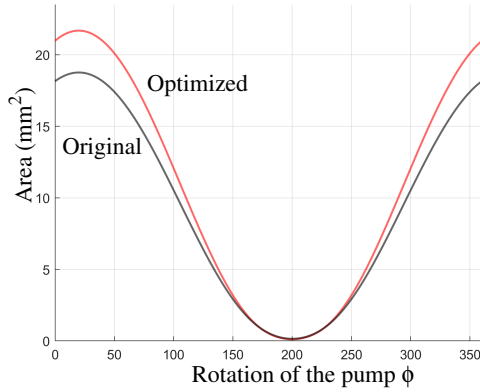
**Figure 26:** *Area evolution for a single compression chamber in the case of the original (black) and optimized profile (red).*

| Z | t(s) | n | $G_{tol}$ |
|---|------|---|-----------|
| 7 | 108.64 | 200 | $10^{-5}$ |
| 8 | 105.73 | 200 | $10^{-5}$ |
| 9 | 102.53 | 200 | $10^{-5}$ |
| 10 | 94.42 | 200 | $10^{-5}$ |

**Table 2:** *Execution times for the search of $P_{opt}$ in Fig. 27. For all runs the number of points on the envelope's tooth profile was set to $n = 200$ and the area constraint tolerance was set to $G_{tol} = 10^{-5}$. This means we allow our result to deviate from the constraint manifold as much as $G_{tol}$.*

### 6.2. Discussions & limitations

*Optimizing the number of teeth.* Even though we did not optimize the number of teeth, it would be possible to consider that parameter also as an optimization variable and use mixed-integer programming to look also for the optimal number of teeth. However, it is in accordance with the engineering practice that the number of teeth is fixed and only the shape of the gerotor is being optimized. The reason for that is that the selection of the number of teeth obeys to factors related to the specific operation of the pump (e.g. operation speed). This variable, however, does affect the wear and contact stress of the workpiece [KRFM12] and common engineering practice dictates that a minimum of $Z = 7$ should be used to ensure correct gearing [JDM16]. Additionally to the gearing factor, pumps with less $Z = 7$ teeth are discouraged in practice due to the flowrate ripple effects, vibrations, and louder noise. See [GMCC19] for a review of articles that elaborate on this matter.

*Alternative optimization methods.* We used interior point and augmented Lagrangian genetic algorithm as our optimization method as it is well suited for optimization with several constraints and has good convergence properties. Alternatively, one could experiment with other genetic algorithms or other evolutionary methods well-suited for non-analytic objective functions [Vos99].

*Other optimization objectives.* We approached the problem purely geometrically, looking for the best shape that maximizes the area of compression chambers, postulating that their size is proportional to the whole flowrate. In our case we were approached by an in-

dustrial partner with a task to optimize for maximum flowrate, but for certain applications one may aim at other objectives, e.g. flowrate steadiness in medical dosing applications, noise reduction, etc. With a modification of the objective function, our framework can be easily adapted towards that goal.

*Physical validations.* We have 3D printed a plastic prototype of the optimized gerotor computed using the proposed algorithm and also the original workpiece to manually test their kinematic behaviour, see Fig. 28. Both mechanisms behave similarly in terms of rotating the interior part inside the exterior base. We have not run physical experiments using a metal workpiece; however, using the help of our industrial partner, we aim to validate the optimization results by physical tests in the future. We add a video of both moving prototypes as complementary material.

*Computational efficiency.* The computational time takes a few minutes to compute the whole algorithm on a standard laptop. Some parts of the algorithm, e.g., the execution of the interior point algorithm could eventually get speeded up via parallelization, however, in the whole gerotor fabrication cycle, this computation time negligible.

### 7. Conclusions

A computational framework to design and optimize gerotor pumps has been presented. The proposed approach constructs a configuration space of all physically feasible gerotors. Considering three major design parameters, the search space is a part of $\mathbb{R}^3$, where the desired gerotor is sought for. The search for the most efficient gerotor is formulated as a constrained optimization problem and an interior-point algorithm is used to find the maximizer. The results show that the proposed framework finds the optimal solution. The proposed algorithm has been tested on an benchmark geometry, showing that the flowrate can be increased up to 16% compared to an existing gerotor.

### References

[AR16]      ALTARE G., RUNDO M.: Computational fluid dynamics analysis of gerotor lubricating pumps at high-speed: geometric features influencing the filling capability. *Journal of Fluids Engineering 138*, 11 (2016), 111101. 2

[BEH11]    BARTOŇ M., ELBER G., HANNIEL I.: Topologically guaranteed univariate solutions of underconstrained polynomial systems via no-loop and single-component tests. *Computer-Aided Design 43*, 8 (2011), 1035–1044. 5

[CGMRC17]  CASTILLA R., GAMEZ-MONTERO P. J., RAUSH G., CODINA E.: Method for fluid flow simulation of a gerotor pump using openfoam. *Journal of Fluids Engineering 139*, 11 (2017), 111101. 2
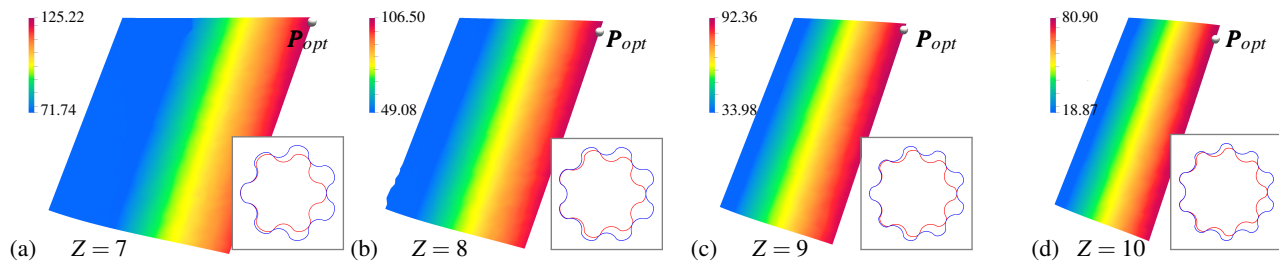
**Figure 27:** *Effect of the number of teeth Z = [7, 8, 9, 10] on the optimum profile $P_{opt}$. The maximum cavity area diminishes as Z increases and the optimum is always located on the e = max border of the constrained manifold $G_f$.*
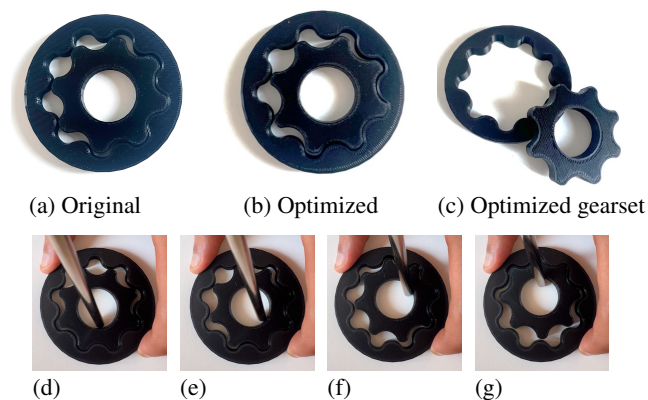


**Figure 28:** *Plastic 3D printed prototypes of the original and optimized workpieces. We verify the kinematic behaviour of both gearsets to ensure movement smoothness. In the second row we show snapshots of the optimized set movement (see also the attached video).*

[CGT97] CONN A., GOULD N., TOINT P.: A globally convergent lagrangian barrier algorithm for optimization with general inequality constraints and simple bounds. *Mathematics of computation 66*, 217 (1997), 261–288. 9

[CKL*12] CHOI T., KIM M., LEE G., JUNG S., BAE J., KIM C.: Design of rotor for internal gear pump using cycloid and circular-arc curves. 2

[Col74] COLBOURNE J.: The geometry of trochoid envelopes and their application in rotary pumps. *Mechanism and Machine Theory 9*, 3-4 (1974), 421–435. 5

[Deb00] DEB K.: An efficient constraint handling method for genetic algorithms. *Computer methods in applied mechanics and engineering 186*, 2-4 (2000), 311–338. 9

[DMJS19] DE MARTIN A., JACAZIO G., SORLI M.: Optimization of gerotor pumps with asymmetric profiles through an evolutionary strategy algorithm. *Machines 7*, 1 (2019), 17. 2

[FMN*99] FABIANI M., MANCÒ S., NERVEGNA N., RUNDO M., AR-MENIO G., PACHETTI C., TRICHILO R.: *Modelling and simulation of gerotor gearing in lubricating oil pumps*. Tech. rep., SAE Technical Paper, 1999. 2

[GMCC19] GAMEZ-MONTERO P. J., CODINA E., CASTILLA R.: A review of gerotor technology in hydraulic machines. *Energies 12*, 12 (2019), 2423. 2, 11

[HH07] HWANG Y.-W., HSIEH C.-F.: Geometric design using hypotrochoid and nonundercutting conditions for an internal cycloidal gear. 2

[IB12] IPPOLITI L., BERTEN O.: Influence of inlet piping conditions on the performance of an aircraft engine lubrication system pump. In *Proceedings of the 9th National Congress on Theoretical and Applied Mechanics, Brussels, Belgium* (2012), Citeseer, pp. 9–10. 2

[IDMC10] IVANOVIC L., DEVEDZIC G., MIRIC N., CUKOVIC S.: Analysis of forces and moments in gerotor pumps. *Proceedings of the Institution of Mechanical Engineers, Part C: Journal of Mechanical Engineering Science 224*, 10 (2010), 2257–2269. 2

[JDM16] JACAZIO G., DE MARTIN A.: Influence of rotor profile geometry on the performance of an original low-pressure gerotor pump. *Mechanism and Machine Theory 100* (2016), 296–312. 11

[KGS15] KLOPSCH V., GERMANN T., SEITZ H.: Numerical simulation of low-pulsation gerotor pumps for use in the pharmaceutical industry and in biomedicine. *Current Directions in Biomedical Engineering 1*, 1 (2015), 433–436. 2

[KKS08] KWON S.-M., KIM M. S., SHIN J.-H.: Analytical wear model of a gerotor pump without hydrodynamic effect. *Journal of Advanced Mechanical Design, Systems, and Manufacturing 2*, 2 (2008), 230–237. 2

[KKS11] KWON S.-M., KIM C.-H., SHIN J.-H.: Optimal rotor wear design in hypotrochoidal gear pump using genetic algorithm. *Journal of Central South University 18* (2011), 718–725. 2

[KPJ00] KIM G.-W., PARK J.-I., JANG J.-D.: *Performance Development for Hydraulic Elements of Hyundai Automotive Automatic Transmission*. Tech. rep., SAE Technical Paper, 2000. 2

[KRFM12] KARAMOOZ RAVARI M., FOROUZAN M., MOOSAVI H.: Flow irregularity and wear optimization in epitrochoidal gerotor pumps. *Meccanica 47* (2012), 917–928. 2, 11

[KSS06] KOVACEVIC A., STOSIC N., SMITH I. K.: Advanced methods and tools for screw compressor design. *Proceedings of the TMCE 2006* (2006). 2

[LF96] LITVIN F. L., FENG P.-H.: Computerized design and generation of cycloidal gearings. *Mechanism and Machine Theory 31*, 7 (1996), 891–911. 2, 8

[LF97] LITVIN F. L., FENG P.-H.: Computerized design, generation, and simulation of meshing of rotors of screw compressor. *Mechanism and Machine Theory 32*, 2 (1997), 137–160. 2

[LF04] LITVIN F. L., FUENTES A.: *Gear geometry and applied theory*. Cambridge University Press, 2004. 2

[LJEK11] LINGESWARAMURTHY P., JAYABHASKAR J., ELAYARAJA R., KUMAR J. S.: Development of analytical model for design of gerotor oil pump and experimental validation. *SAE International Journal of Engines 4*, 1 (2011), 441–449. 2

[LKSK18] LEE M.-C., KWAK H.-S., SEONG H.-S., KIM C.: A study on theoretical flowrate of gerotor pump using chamber areas. *International*

*Journal of Precision Engineering and Manufacturing 19* (2018), 1385–1392. 8

[LSTS*14]  LEESTER-SCHÄDEL M., THIES J.-W., SCHUBERT T., BÜTTGENBACH S., DIETZEL A.: Rotational micro actuator for microsurgery. *Microsystem technologies 20* (2014), 879–888. 2

[McN74]  MCNEIL I.: Hydraulic power transmission: The first 350 years. *Transactions of the Newcomen Society 47*, 1 (1974), 149–159. 2

[MMRN00]  MANCÒ G., MANCÒ S., RUNDO M., NERVEGNA N.: Computerized generation of novel gearings for internal combustion engines lubricating pumps. *International Journal of Fluid Power 1*, 1 (2000), 49–58. 3

[MSE20]  MACHCHHAR J., SEGERMAN H., ELBER G.: Conjugate shape simplification via precise algebraic planar sweeps toward gear design. *Computers & Graphics* (2020). 3

[PBS89]  PENNOCK G. R., BEARD J. E., STANISIC M. M.: The effects of the design parameters on the generated curvature and displacement of epitrochoidal gerotor pumps. *SAE transactions* (1989), 217–228. 2

[PP00]  POTTMANN H., PETERNELL M.: Envelopes-computational theory and applications. In *Spring conference on computer graphics* (2000), pp. 3–23. 4, 6

[PVF*17]  PELLEGRI M., VACCA A., FROSINA E., BUONO D., SENATORE A.: Numerical analysis and experimental validation of gerotor pumps: A comparison between a lumped parameter and a computational fluid dynamics-based approach. *Proceedings of the Institution of Mechanical Engineers, Part C: Journal of Mechanical Engineering Science 231*, 23 (2017), 4413–4430. 2

[RN15]  RUNDO M., NERVEGNA N.: Lubrication pumps for internal combustion engines: a review. *International Journal of Fluid Power 16*, 2 (2015), 59–74. 2

[Run17]  RUNDO M.: Models for flow rate simulation in gear pumps: A review. *Energies 10*, 9 (2017), 1261. 2, 10

[RV18]  ROBISON A., VACCA A.: Multi-objective optimization of circular-toothed gerotors for kinematics and wear by genetic algorithm. *Mechanism and Machine Theory 128* (2018), 150–168. 2

[RV19]  ROBISON A., VACCA A.: *Multi-Objective Optimization of Gerotor Port Design by Genetic Algorithm with Considerations on Kinematic vs. Actual Flow Ripple*. Tech. rep., SAE Technical Paper, 2019. 2

[RV21]  ROBISON A. J., VACCA A.: Performance comparison of epitrochoidal, hypotrochoidal, and cycloidal gerotor gear profiles. *Mechanism and Machine Theory 158* (2021), 104228. 2, 3

[SAJ21]  SELLÁN S., AIGERMAN N., JACOBSON A.: Swept volumes via spacetime numerical continuation. *ACM Transactions on Graphics (TOG) 40*, 4 (2021), 1–11. 3

[SH03]  STEWART B. A., HOWELL T.: *Encyclopedia of Water Science (Print)*. CRC press, 2003. 2

[SSKM11]  STOSIC N., SMITH I. K., KOVACEVIC A., MUJIC E.: Geometry of screw compressor rotors and their tools. *Journal of Zhejiang University-SCIENCE A 12*, 4 (2011), 310–326. 2, 3

[Vos99]  VOSE M. D.: *The simple genetic algorithm: foundations and theory*. MIT press, 1999. 11

[WMNO06]  WALTZ R. A., MORALES J. L., NOCEDAL J., ORBAN D.: An interior algorithm for nonlinear optimization that combines line search and trust region steps. *Mathematical programming 107*, 3 (2006), 391–408. 9

[XFS*20]  XU H., FU T., SONG P., ZHOU M., MITRA N., CHI-WING F.: Computational design and optimization of non-circular gears. *Computer Graphics Forum* (2020). 3

[YYT09]  YAN J., YANG D. C., TONG S.-H.: A new gerotor design method with switch angle assignability. 2

[Zha10]  ZHANG P.: *Advanced industrial control technology*. William Andrew, 2010. 6